POST-MAIN SEQUENCE EVOLUTION. II: MASSIVE STARS

15.1 Introduction

We saw in Lecture 13 that low- and intermediate-mass stars (with $M \leq 8M_\odot$) develop carbon-oxygen cores that become degenerate after central He burning. The electron degenerate pressure supports the core against further collapse; as a consequence, the maximum core temperature reached in these stars is lower than the $T \simeq 6 \times 10^8$ K required for carbon fusion (Lecture 7.4.4). During the latest stages of evolution on the AGB, these stars undergo strong mass loss which removes the remaining envelope, leaving as their remnants cooling C-O white dwarfs.

The evolution of *massive* stars differs in two important respects from that of low- and intermediate-mass stars:

(1) Massive stars undergo *non-degenerate carbon ignition* in their cores. The minimum CO *core* mass for this to happen at the end of core He burning has been estimated with detailed modelling to be $M_{\rm CO-core} > 1.06M_\odot$. The corresponding ZAMS *stellar* mass is somewhat uncertain mainly due to uncertainties related to mixing (e.g. convective overshooting), but is considered to be $\sim 8M_\odot$. This is why $M = 8M_\odot$ is conventionally taken as the boundary between 'intermediate' and 'high' mass stars.

Stars with $M \gtrsim 11M_\odot$ achieve core temperatures high enough to ignite and burn elements heavier than carbon up to and including Fe which is near the peak of the binding energy per nucleon curve (Figure 7.2). With no more nuclear energy to be extracted by burning Fe, the Fe core collapses leading to a '*core-collapse supernova*' (Lecture 16). Just before exploding as a supernova, a massive star has an 'onion skin' internal structure (Figure 15.1)

(2) Whereas low- and intermediate-mass stars experience mass loss during the late stages of their evolution, when they are on the RGB and AGB (Lecture 13), for stars with masses $M \gtrsim 15M_\odot$, mass loss by fast and en-

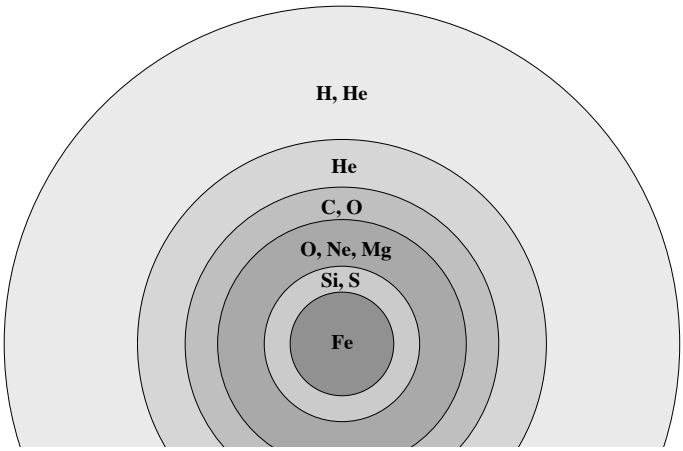

Figure 15.1: Schematic overview of the 'onion skin' structure of a massive star at the end of its evolution.

ergetic stellar winds is important during all evolutionary phases, including the main sequence. For $M \gtrsim 30 M_{\odot}$, the mass-loss rates $\dot{M}$ are so large that the timescale for mass loss, $t_{\rm ml} = M/\dot{M}$ because smaller than the nuclear timescale $t_{\rm nuc}$. Therefore mass loss has a very significant effect on the evolution of these stars, introducing substantial uncertainties in the calculations of massive star evolution.

Mass loss peels off the outer layers of a star, revealing at the stellar surface the products of nuclear burning brought up into higher layers by convective overshooting. Thus the photospheric abundances are changed drastically. The combination of mass reduction in the outer layers on the one hand, and larger core size—and hence increased luminosity—as a result of convective overshooting on the other, makes all massive stars overluminous for their masses. The main sequence lifetime is also increased because of the larger core size.

We look in more detail at the properties of stellar winds in Section 15.3.

15.2 Massive Stars in the H-R Diagram

The evolutionary journey through the H-R diagram of a massive star undergoing the different phases of core and shell burning that lead to the internal structure shown in Figure 15.1 is complicated. Figure 15.2 shows examples of evolutionary tracks for stars of solar metallicity, calculated with computer-generated models that include mass loss and convective

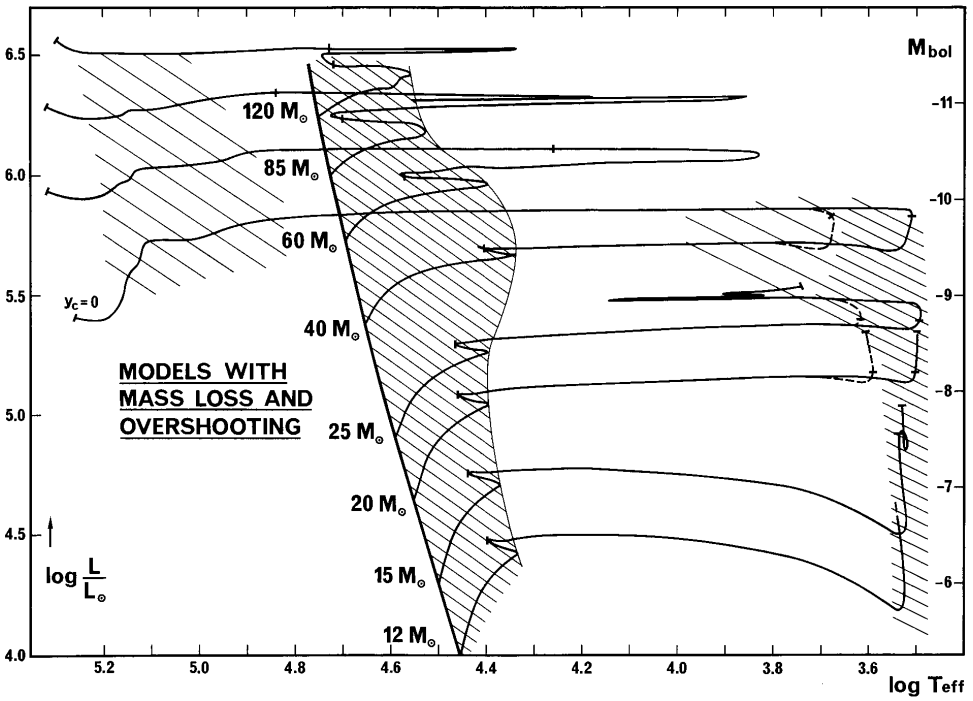

Figure 15.2: Evolutionary tracks of massive stars calculated with mass loss and a moderate amount of convective overshooting. The shaded regions correspond to long-lived evolutionary phases: (i) on the main sequence; (ii) during core He burning as a Red Supergiant (RSG) at $\log T_{\rm eff} < 4.0$; and (iii) as a Wolf-Rayet (WR) star at $\log T_{\rm eff} > 4.8$. Stars with $M_{\rm ZAMS} > 40 M_\odot$ are assumed to lose their entire envelope during the Luminous Blue Variable (LBV) phase and never become RSGs. (Figure reproduced from Maeder & Meynet 1987, A&A 182, 243).

overshooting. More recent developments of the code used by the same authors also include the effects of stellar rotation and consider a range of metallicities.

As the core and shell energy sources vary in relative strength, the star makes a number of excursions to and fro across the HR diagram. In high-mass stars, these rightward (core exhaustion) and leftward (core ignition) excursions, between the red and blue (supergiant) branches respectively, occur with only a slight systematic increase in luminosity. Thus, the evolutionary tracks of high-mass stars are close to horizontal in the H-R diagram. In very high-mass stars, the nuclear evolution in the central regions of the star occurs so quickly that the outer layers have no time to respond to the successive rounds of core exhaustion and core ignition, and there is only a relatively steady drift to the right on the H-R diagram before the star arrives at the pre-supernova state shown in Figure 15.1.

The path followed by evolving massive stars in the upper part of the H-R

diagram gives rise to a rich nomenclature. On the main sequence, stars with $M_{\rm ZAMS} \gtrsim 20 M_\odot$ are of spectral type O. They evolve off the main sequence as blue and red supergiants (BSG and RSG). Of stars are very massive O supergiants whose spectra show pronounced emission lines. The most massive stars evolve into Luminous Blue Variables (LBVs) which have already encountered in Lecture 10.6.1.

Stars with $M \lesssim 40 M_\odot$ spend a large fraction of their core He-burning phase as red supergiants. During this phase, a large part or even the entire envelope can be evaporated by the stellar wind, exposing the helium core of the star as a Wolf-Rayet (WR) star. WR stars are extreme objects which continue to attract a great deal of attention by stellar astronomers. We describe their main characteristics below.

15.2.1 Wolf-Rayet Stars

Spectroscopically, WR stars are spectacular in appearance: their optical and UV spectra are dominated by strong, broad emission lines instead of the narrow absorption lines that are typical of 'normal' stars (Figure 15.3). The emission lines are so strong that they were first noticed as early as 1867 by... Charles Wolf and Georges Rayet (!) using the 40 cm Foucault telescope at the Paris Observatory. Nowadays, this characteristic is exploited to identify WR stars in external galaxies with narrow-band imaging. After some debate, which lasted into the 1970s, WR are now recognised as the evolved descendent of O-type stars, whose H or He-burning cores have been exposed as a result of substantial mass loss.

From the earliest stages of the subject, it was clear that WR come in two flavours: those with strong emission lines of He and N (WN subtypes), and those with strong He, C and O lines (WC and WO subtypes), in which the products of, respectively, the CNO cycle and triple-α nuclear reactions are revealed. Each class is further subdivided in subclasses. WN2 to WN5 are early WN, or WNE, WN7 to WN9 are late WN or WNL, with WN6 being referred to as either early or late. The classification is based on the relative strengths of emission lines of N III to N V and He I to He II (see Figure 15.3). Similarly, WC and WO subtype classification is based on the ratios of highly ionised C and O emission lines.

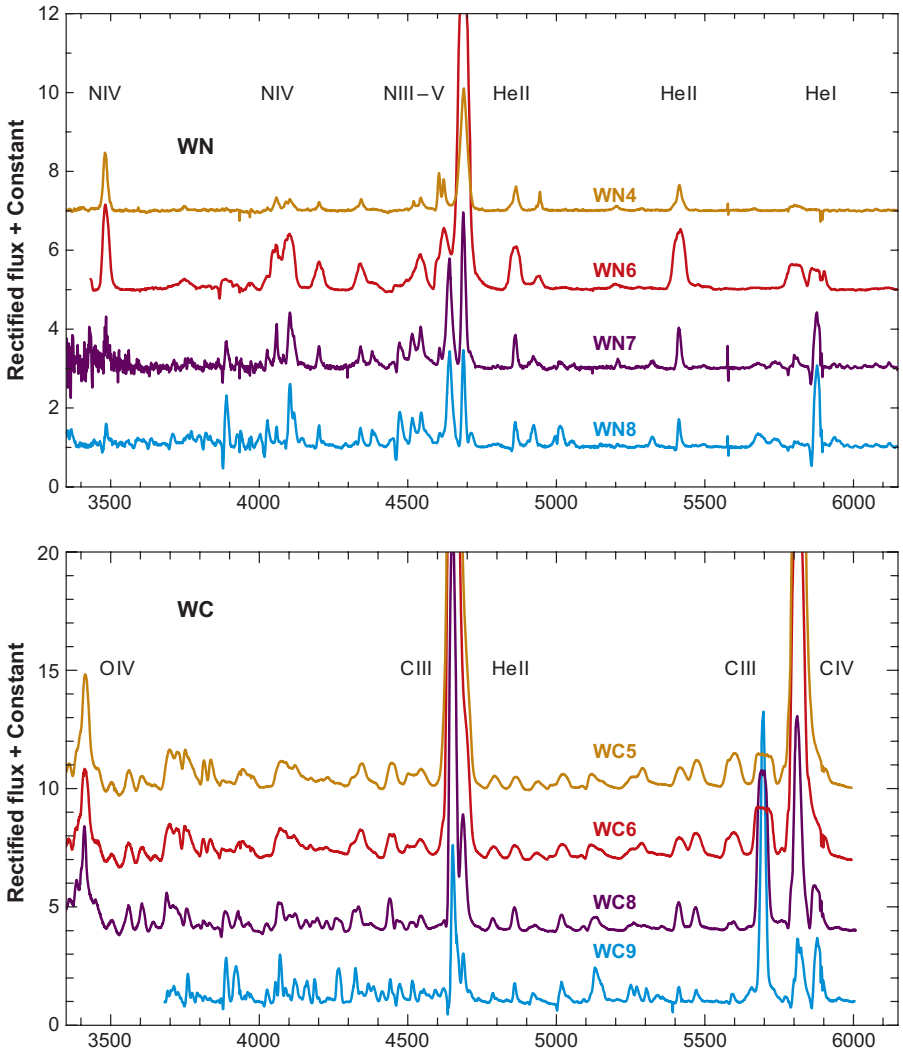

Figure 15.3: Examples of optical spectra of Galactic Wolf-Rayet stars of the WN and WC classes. The x-axis is wavelength is Å. (Figure reproduced from Crowther 2007, ARAA, 45, 177).

When these spectral characteristics are interpreted in terms of the surface abundances, the following picture emerges:

WNL stars have H present on their surfaces (with $X < 0.4$) and increased He and N abundances, consistent with equilibrium values from the CNO cycle;

WNE stars are similar to WNL stars in terms of their He and N abundances, but lack H ($X = 0$);

WC stars have no H, little or no N, and increased He, C and O abundances (consistent with partial He-burning);

WO stars are similar to WC stars with strongly increased O abundances (as expected for nearly complete He-burning).

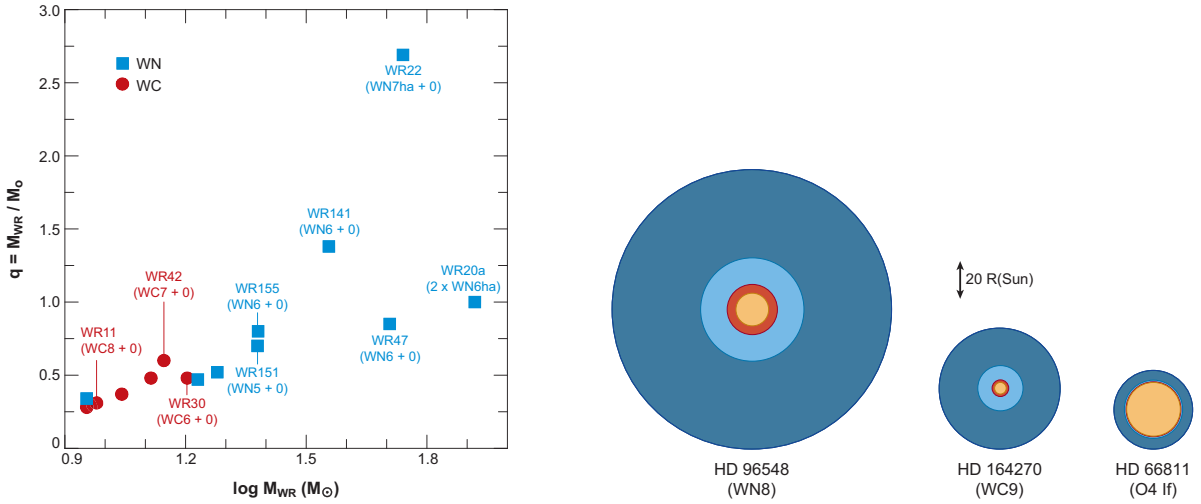

Figure 15.4: *Left:* Stellar masses of Galactic Wolf-Rayet stars ($M_{\rm WR}$) deduced from the analysis of binary orbits. The y-axis is the ratio of the WR mass to that of its binary companion, usually an O-type star. *Right:* Stellar radii at Rosseland optical depths of 20 (*orange*) and 2/3 (*red*) for an O4 If, a WC9, and a WN8 star, shown to scale. The primary optical emission line region is shown in dark blue, with light blue indicating higher density wind material. WR stars have much more extended winds than Of supergiants. (Figures reproduced from Crowther 2007, ARAA, 45, 177).

Approximately 40% of WR stars in the Milky Way occur in binary systems, allowing their masses to be measured (Lecture 4). As can be seen from Figure 15.4, WCs span a relatively narrow mass range, from 9 to $16 M_\odot$, whereas WN masses are found between ~ 10 and $83 M_\odot$, and in some cases exceed the mass of their OB companions, i.e. $M_{\rm WR}/M_{\rm O} > 1$.

The strong, broad emission lines characteristic of WR stars are due to their powerful stellar winds, with terminal velocities as high as $v_\infty \simeq 2000\,{\rm km\ s^{-1}}$ and mass loss rates as high as $\dot{M} \simeq 10^{-5} M_\odot\ {\rm yr}^{-1}$. WR winds are sufficiently dense that an optical depth of unity in the continuum arises in the outflowing material (rather than in a stationary stellar photosphere, as in 'normal' stars). The emission lines are formed far out in the wind; both line- and continuum-emitting regions are much larger than the conventional stellar radius (Figure 15.4, right panel), and their physical depths are highly wavelength dependent.

Some young WR stars, mostly WNs, are surrounded by spectacular ring nebulae, thought to be the result of the interaction between material ejected in a slow wind by the WR precursor and the WR fast wind. The hard radiation from the central WR star photoionises the swept-up circumstellar gas, producing a wind-blown bubble. In OB associations containing

many massive stars, the combined effects of stellar winds and the supernova explosions that mark the ends of the lives of stars more massive than $8M_\odot$ can produce *'superbubbles'*.

15.2.2 The Conti Evolutionary Scenario

In 1976, Peter Conti proposed an evolutionary scenario that links the various types of massive stars which, until then, had been classified primarily on the basis of the appearance of their spectra.

$M \lesssim 15\,M_\odot$	MS (OB) → RSG (→ BSG in blue loop? → RSG) → SN II mass loss is relatively unimportant, $\lesssim$ few $M_\odot$ is lost during entire evolution
$15\,M_\odot \lesssim M \lesssim 25\,M_\odot$	MS (O) → BSG → RSG → SN II mass loss is strong during the RSG phase, but not strong enough to remove the whole H-rich envelope
$25\,M_\odot \lesssim M \lesssim 40\,M_\odot$	MS (O) → BSG → RSG → WNL → WNE → WC → SN Ib the H-rich envelope is removed during the RSG stage, turning the star into a WR star
$M \gtrsim 40\,M_\odot$	MS (O) → BSG → LBV → WNL → WNE → WC → SN Ib/c an LBV phase blows off the envelope before the RSG can be reached

These evolutionary sequences are still being refined. The relation of the final evolutionary stage to the supernova types indicated above will be clarified in Lecture 16.

The limiting masses given above are only indicative, and apply (approximately) to massive stars of solar metallicity. However, mass-loss rates decrease with decreasing Z because, as we shall see presently (Section 15.3 and following), stellar winds are driven by the absorption of photons by metal lines. Thus, the mass limits are higher for stars of lower metallicity.

The metallicity dependence of the winds from massive stars is thought to be the fundamental reason behind the empirical observation that the frequency of WR stars and the breakdown between different WR subclasses are not the same in all galaxies. The best sampled galaxies are the Milky Way ($Z = Z_\odot$), the LMC ($Z \simeq 1/2Z_\odot$) and the SMC ($Z \simeq 1/6Z_\odot$), although with large telescopes the samples are now being extended to other galaxies (see the recent review by Neugent & Massey 2019). In the solar neighbourhood, the ratio of WR stars to their O progenitors is

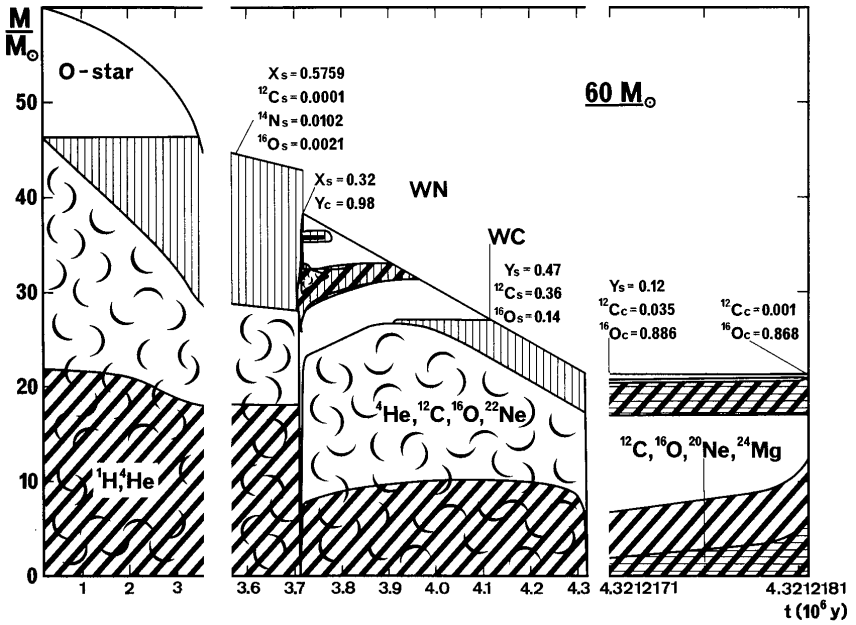

Figure 15.5: Diagram of the evolution of a $60 M_\odot$ star of solar metallicity. Cross-hatched areas indicate where nuclear burning occurs, and curly symbols indicate convective regions. (Figure reproduced from Maeder & Meynet 1987, A&A 182, 243).

N(WR)/N(O) $\sim$ 0.15, but in the SMC N(WR)/N(O) $\simeq$ 12/1000 = 0.01. Furthermore, in the solar neighbourhood N(WN) $\simeq$ N(WC), but in the LMC N(WN)/N(WC) $\simeq$ 5 and in the SMC N(WN)/N(WC) $\sim$ 10.

Figure 15.5 illustrates the evolutionary scenario for a $M = 60 M_\odot$ star, indicative of the most massive stars. After $\sim$ 3.5 Myr, while the star is still on the main sequence, mass loss exposes layers that formerly belonged to the (large) convective core. Thus CNO-cycling products, especially N, are revealed, and the surface He abundance increases at the expense of H. During the very short phase between core H and He burning ($t = 3.7$ Myr), several $M_\odot$ are rapidly lost in an LBV phase. During the first part of core He burning ($t = 3.7$–3.9 Myr), the star appears as a WNL star, and subsequently ($t = 3.9$–4.1 Myr) as a WNE star, after mass loss has removed the last H-rich layers outside the H-burning shell. After 4.1 Myr, material that was formerly in the He-burning convective core is exposed at the surface: N, which was consumed in He-burning reactions, disappears while the products of He-burning, C and O, appear. In the last 0.2 Myr of its evolution the star is a WC star.

In general, mass loss rates during all evolutionary phases increase with stellar mass; as a result, there is a convergence of the final (pre-supernova) masses to a range between 5 and 10 $M_\odot$. However, this effect is diminished in metal-poor stars which experience lower mass loss rates.

Table 15.1 summarises some of the properties of the different nuclear burning stages in a $15M_\odot$ star. Note the accelerating timescales as heavier and heavier elements are ignited and the star approaches its final fate as a supernova.

Table 15.1. Properties of nuclear burning stages in a 15 $M_\odot$ star (from Woosley et al. 2002).

burning stage	T (10^9 K)	ρ (g/cm^3)	fuel	main products	timescale
hydrogen	0.035	5.8	H	He	1.1×10^7 yr
helium	0.18	1.4×10^3	He	C, O	2.0×10^6 yr
carbon	0.83	2.4×10^5	C	O, Ne	2.0×10^3 yr
neon	1.6	7.2×10^6	Ne	O, Mg	0.7 yr
oxygen	1.9	6.7×10^6	O, Mg	Si, S	2.6 yr
silicon	3.3	4.3×10^7	Si, S	Fe, Ni	18 d

15.3 Stellar Winds

Most stars lose mass. The existence of the *solar wind*, a stream of high velocity particles moving radially outwards from the Sun and carrying magnetic fields with them, was inferred in the early 1950s from the observation that comet ion tails always point away from the Sun, rather than trailing behind the comet. The total mass flow can be estimated from the particle density and their typical velocity (at the location of the Earth):

$$\dot{M} = n\, m_H\, v\, 4\pi d^2 \sim 10^{-14} M_\odot \text{ yr}^{-1} \tag{15.1}$$

where $d = 1\,\text{AU}$, $n \sim 5\,\text{cm}^{-3}$, and $v \sim 500\,\text{km s}^{-1}$. With such a low mass loss rate, the Sun will have lost only $\sim 0.1\%$ of its mass during its entire lifetime of $\sim 10^{11}$ years (if the present mass-loss rate remained constant during the whole lifetime of the Sun, which it won't, as we saw in Lecture 13).

The mechanism by which solar mass stars lose mass is quite different from that which drives the much higher mass loss rates ($\dot{M} = 10^{-7}$–$10^{-4} M_\odot$ yr^{-1}, corresponding to $\sim 1/30$ to 30 Earth masses per year) seen in hot stars with $M \gtrsim 15M_\odot$ and which we are going to discuss here.

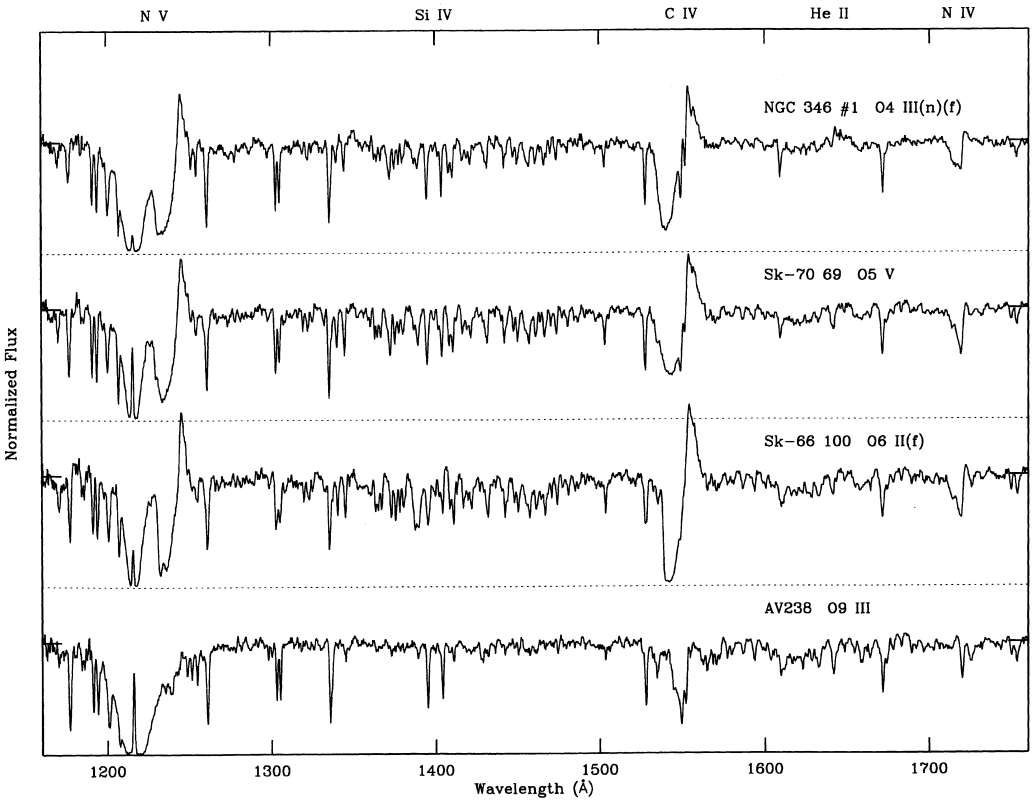

Figure 15.6: Ultraviolet spectra of massive OB stars in the Magellanic Clouds, obtained with the Faint Object Spectrograph on the *Hubble Space Telescope*. The resonance lines of N V $\lambda\lambda$1238, 1242 and C IV $\lambda\lambda$1548, 1550 display strong P Cygni profiles indicative of high wind terminal velocities and large mass loss rates. (Figure reproduced from Walborn et al. 1995, PASP, 107, 104).

15.3.1 P Cygni Line Profiles

We see *direct* evidence of such mass loss in the profiles of spectral lines of highly ionised species such as C IV, Si IV, N V and O VI in the ultraviolet spectra (from 1549 to 1035 Å) of primarily O and B-type stars (but also WR stars and A supergiants); some examples are shown in Figure 15.6.

These line profiles, which are a mixture of emission and absorption, are called P Cygni profiles from the LBV star in which they were first seen. Figure 15.7 illustrates the basic formation mechanism in an *outflowing extended* stellar atmosphere.

The material in front of the stellar disk absorbs light at the frequencies of these resonance lines. The resulting absorption profile extends from $v = 0\,\mathrm{km\ s^{-1}}$ (assuming the radial velocity of the star relative to the Earth to be zero) to a maximum *negative* velocity, v_∞. Thus, the absorption line has a net *blue*-shift relative to the star. Although absorption of starlight

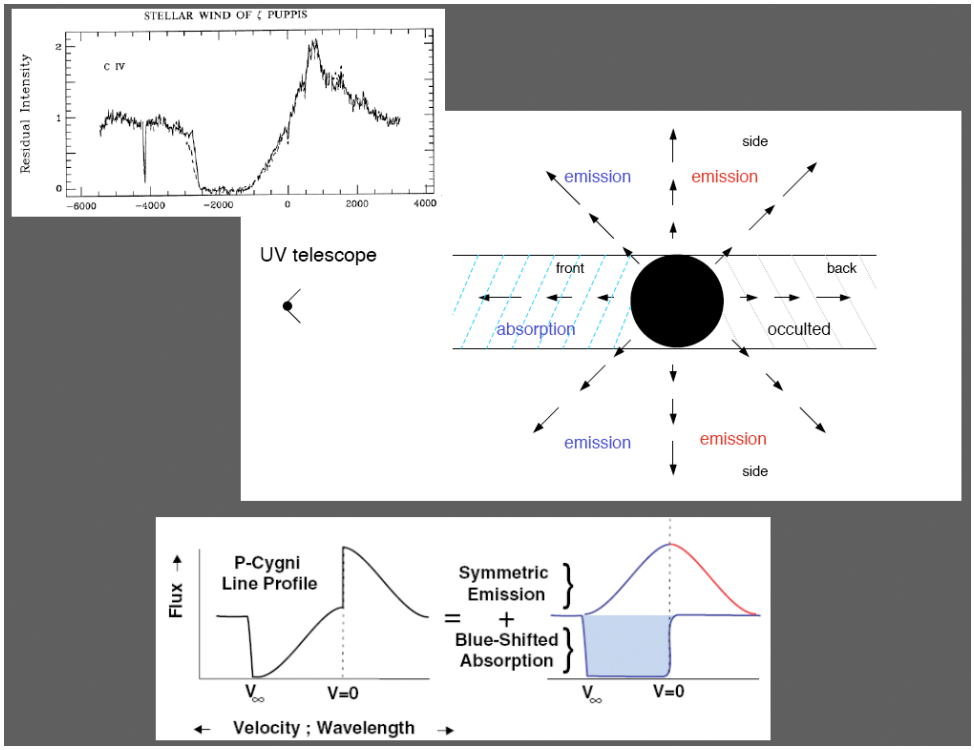

Figure 15.7: Schematic representation of the origin of P Cygni line profiles in an expanding stellar atmosphere.

takes place everywhere within the extended atmosphere, we can only see it if the absorbing ions are located in front of the stellar disk—hence the net blueshift of the absorption component of the P Cygni profile.

Once the outflow reaches its maximum velocity, this velocity will remain approximately constant up to large distances from the star (in the absence of other forces); hence the term *'terminal velocity'*. Typical values range from $v_\infty \simeq -200\,\mathrm{km\ s^{-1}}$ in A-type supergiants to $v_\infty \simeq -3000\,\mathrm{km\ s^{-1}}$ in early O-type stars. The sound speeds in the atmospheres of these stars are typically 10–30 $\mathrm{km\ s^{-1}}$; thus the winds are highly *supersonic*.

If the material in front of the star is optically thick over the full velocity range, it will produce strongly saturated, almost rectangular, absorption line profiles, as in the example shown in Figure 15.7. This is not necessarily always the case, and weaker, unsaturated absorption components to the P Cygni composite profile are possible.

Following absorption in any of the above resonant (from the ground state to the first excited level of the ion under consideration) lines, a new photon will be re-emitted as the electron returns to the ground state. Overall, an observer would see an emission profile resulting from a multitude of such

re-emission processes at different velocities. Note that the wind emission provides additional radiation over that due to the stellar photosphere's blackbody emission; that is, we see an emission line superimposed on the stellar continuum.

Unlike the absorption case, an observer sees photons emitted from gas behind, as well as in front of, the star—gas that is moving with, respectively, positive and negative velocities relative to the star. Such an emission profile has a maximum at $v = 0$ and falls off to zero at v_∞. This is simply a geometrical effect, with the largest emitting areas having net zero velocity (projected along the line of sight to the observer). The larger the projected wind velocity, the smaller the corresponding emitting area. Since there are no absorbing and re-emitting ions at velocities larger than v_∞, the emission profile is restricted to this velocity range.

Note that if the radius of the stellar photosphere (where the continuum in produced) is not small compared to the physical extent of the wind, the emission profile can be intrinsically asymmetric, with the approaching, blue-shifted, portion in front of the star emitting more flux (as viewed from a given direction) than the receding back portion which is occulted by the star.

The overall P Cygni profile, as observed for example in the C IV $\lambda\lambda$1548, 1550 lines in the ultraviolet spectrum of the O5 Iaf star ζ Puppis (Figure 15.7), is the superposition of three components: stellar blackbody continuum, blueshifted absorption, and (possibly asymmetric) emission.

15.3.2 Diagnostics of P Cygni Profiles

There are three main physical quantities that can be determined from the analysis of the P Cygni profiles of UV absorption lines in the spectra of hot, massive stars:

(i) The terminal velocity, v_∞. Provided there is a sufficiently high column density of absorbing ions over the full velocity range of the wind, v_∞ can be readily deduced by measuring the extreme blue wavelength of the absorption profile and applying the familiar Doppler formula:

$$v_\infty = \frac{\lambda_{\rm min} - \lambda_0}{\lambda_0}\, c$$

where λ_0 is the laboratory wavelength of the transition under consideration and c is the speed of light.

(ii) The ion column density, N. Provided the absorption profile is not saturated (recall the discussion of this point in Lecture 6.4), it may be possible to deduce the distribution of ion column densities at different velocities in the wind. This is normally done by comparing a family of computer-generated theoretical line profiles with the observed one, and minimising the difference between the two. Under favourable circumstances, the ion column densities thus deduced can be interpreted to infer the mass loss rate and relative element abundances.

(iii) The shape of the velocity field, $v(r)$. Particularly when the absorption profile is saturated, the exact shape of the absorption+emission composite is sensitive to the velocity field—changing the way v varies with distance r from the stellar 'surface' (for example, a steep or a shallow velocity gradient) can produce recognisable changes in the overall P Cygni profile. We shall show some examples in the next section.

15.4 Theory of Radiatively Driven Winds

In this section we shall take a closer look at radiative line acceleration in hot star winds. In particular, we'll see how this acceleration mechanism leads to certain scaling relations for some of the wind properties, such as $\dot{M}$ and v_∞. We consider the simplest possible model: *a homogeneous, time-independent,*[1] *spherically symmetric, stellar wind free of magnetic fields.* We further assume that the photons emitted from the stellar photosphere and which are driving the wind are propagating only radially. None of these simplifying assumption actually applies to real hot star winds, of course. However, it turns out that the majority of observations can be reproduced satisfactorily with such a simple model, except for the assumption of homogeneity (that is, introducing *clumping* in the wind turns out to be important).

[1] Confusingly, in the literature the assumption that the wind properties are time-independent is referred to as a 'stationary' wind.

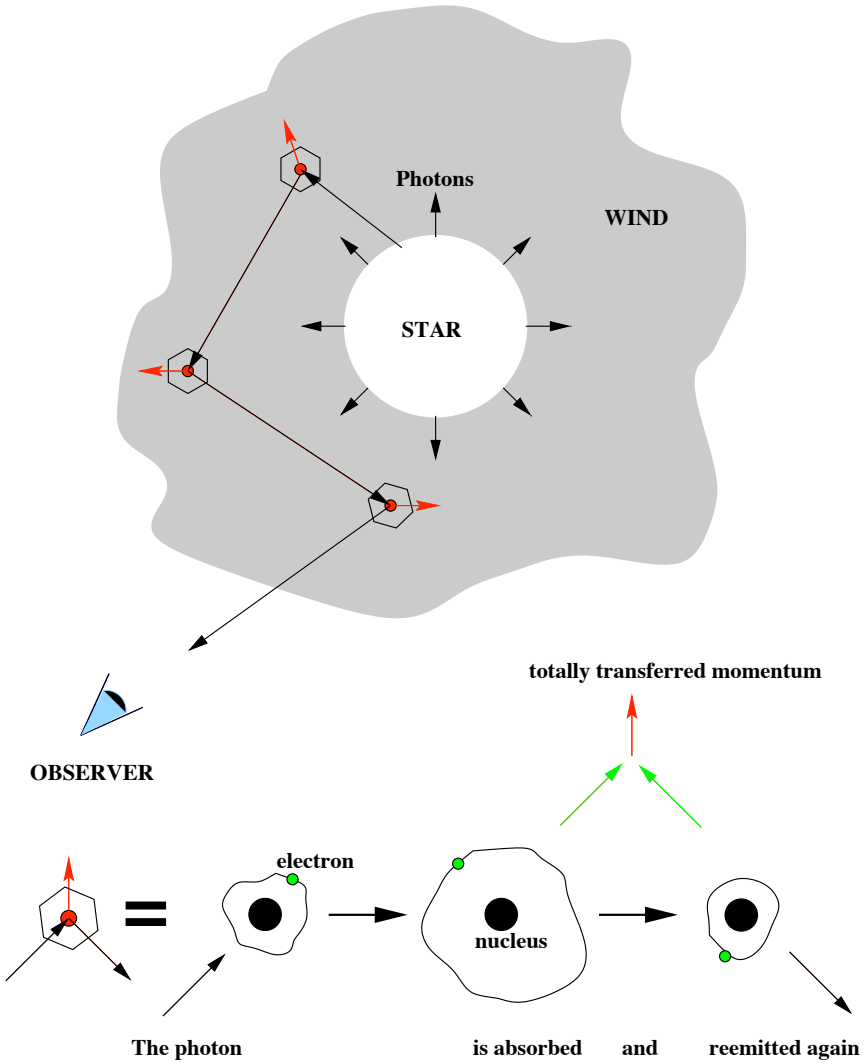

Figure 15.8: Schematic representation of the principle of radiative line-driven winds. Each absorbed photon transmits a momentum $h\nu/c$ to the absorbing ion in the direction of propagation of the photon. The emitted photons transmit a momentum in the direction opposite to the propagation direction. The momenta transmitted by the isotropically re-emitted photons cancel on average. The momenta of the absorbed photons add.

15.4.1 Momentum Transfer via Line Absorption and Re-emission

The basic principle is illustrated in Figure 15.8. The absorption and re-emission of stellar photons in a spectral line with frequency $\nu_{\rm i}$ in the atomic rest frame, result in a net transfer of momentum in the radial direction

$$\Delta P_{\rm radial} = \frac{h}{c}\,(\nu_{\rm in}\cos\theta_{\rm in} - \nu_{\rm out}\cos\theta_{\rm out}) \qquad (15.2)$$

to the absorbing and re-emitting ion. Here θ is the angle between the direction of the photon and the radial unit vector (parallel to the velocity vector) of the ion. Since the absorbed photons are re-emitted isotropically,

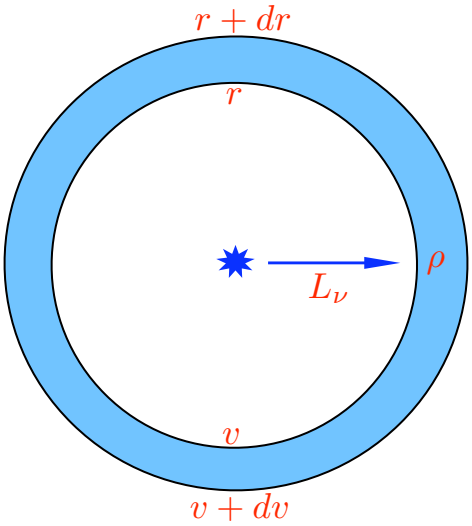

Figure 15.9: Sketch of a blue supergiant star irradiating a thin shell of wind material. L_ν is the star luminosity at frequency ν, v is the wind velocity at radius r, and ρ is the local density within the shell. The shell has mass $m = 4\pi r^2 \rho \, \mathrm{d}r$.

we have:

$$\langle \cos\theta_{\rm out} \rangle = 0 \, . \tag{15.3}$$

On the other hand, prior to absorption the stellar photons are approaching from the direction of the star, that is their direction of propagation is parallel to the ion velocity vector; thus:

$$\langle \cos\theta_{\rm in} \rangle \approx 1 \, . \tag{15.4}$$

Therefore,

$$\langle \Delta P_{\rm radial} \rangle = \frac{h\nu_{\rm in}}{c} \tag{15.5}$$

Let us now consider a thin shell in the wind, as in Figure 15.9. Within the shell, the wind velocity increases by an amount $\mathrm{d}v$ on a scale $\mathrm{d}r$. Photons emitted from the stellar surface (photosphere) with observer's frame frequency $\nu_{\rm obs}$ can be absorbed by an ion if their frequency in the *ion* frame equals the transition frequency $\nu_{\rm i}$. Assuming that the photons propagate radially, the two frequencies are related via the Doppler formula:

$$\begin{aligned} \nu_{\rm i} &= \nu_{\rm obs} - \frac{\nu_{\rm i}}{c} v \\ \nu_{\rm i} &= (\nu_{\rm obs} + \mathrm{d}\nu_{\rm obs}) - \frac{\nu_{\rm i}}{c} (v + \mathrm{d}v) \, . \end{aligned} \tag{15.6}$$

In other words, a possible absorption and re-emission process (which from now on we shall call a 'scattering' event) by an ion moving outwards with the wind requires stellar photons which have left the stellar surface with

higher frequencies than that of the atomic transition under consideration. The frequency interval $\mathrm{d}\nu_{\mathrm{obs}}$ corresponding to the velocity interval $\mathrm{d}v$ is just:

$$\mathrm{d}\nu_{\mathrm{obs}} = \nu_{\mathrm{i}} \frac{\mathrm{d}v}{c} .$$

The radiative acceleration of the shell resulting from a given absorption line can be calculated using the general definition of any acceleration:

$$g^{\mathrm{i}}_{\mathrm{rad}} = \frac{\Delta P}{\Delta t \, \Delta m} . \tag{15.7}$$

In our case, the line acceleration is obtained by multiplying the average momentum transferred in a scattering event by the number of available photons in the corresponding frequency interval, per unit time and per unit mass of the accelerated shell. The number of photons per unit time is simply:

$$\frac{N_\nu}{\Delta t} = \frac{\Delta \left(E_\nu / h\nu \right)}{\Delta t} = \frac{L_\nu \, \Delta\nu_{\mathrm{obs}}}{h\nu_{\mathrm{obs}}} \tag{15.8}$$

where L_ν is the stellar luminosity (equal to the radiated energy per unit time per unit frequency) at frequency ν. With $\nu_{\mathrm{in}} = \nu_{\mathrm{obs}}$, the radial acceleration of the shell caused by a single atomic transition is therefore:

$$g^{\mathrm{i}}_{\mathrm{rad}} = \frac{N_\nu \left\langle \Delta P_{\mathrm{radial}} \right\rangle}{\Delta t \, \Delta m} = \frac{L_\nu \, \Delta\nu_{\mathrm{obs}}}{h\nu_{\mathrm{obs}}} \frac{h\nu_{\mathrm{obs}}}{c} \frac{1}{\Delta m} = \frac{L_\nu \nu_{\mathrm{i}}}{c^2} \frac{\mathrm{d}v}{\mathrm{d}r} \frac{1}{4\pi r^2 \rho} . \tag{15.9}$$

It is noteworthy that the radiative line acceleration of the shell depends on the velocity gradient $\mathrm{d}v/\mathrm{d}r$ within the shell (can you see why?).

15.4.2 Total Line Acceleration

To obtain the total radiative acceleration we need to take into account two other factors.

First, until now we have assumed a unit probability of interaction between photons (of the appropriate frequency) and ions. We include in eq. (15.9) a factor which reflects the dependence of this probability on the atomic properties:

$$\mathcal{P}_{\mathrm{inter}} = 1 - e^{-\tau}$$

where τ is the optical depth of the observed transition at coordinates r, v, $\mathrm{d}v$.

Recalling again our treatment of absorption lines in Lecture 6, we can reduce $\mathcal{P}_{\rm inter}$ to two limiting cases. If $\tau \gg 1$, the atomic transition in question is optically thick, and $\mathcal{P}_{\rm inter} \approx 1$. On the other hand, if $\tau \lesssim 1$, the line is optically thin and the acceleration due to such lines needs to be modified by a factor corresponding to the local optical depth. If $\tau \ll 1$, $\mathcal{P}_{\rm inter} \approx \tau$. The radiative acceleration due to an optically thin line is a factor of τ smaller than that due to an optically thick line.

Second, in the expanding atmosphere of a hot star, there is not just a single atomic transition capable of driving a wind. On the contrary, there are literally millions of transitions from atoms and ions of the most abundant elements of the Periodic Table which are potentially capable of absorbing radiation and momentum. In practice, 'only' some ten thousand lines are relevant for calculating the overall line acceleration, $g_{\rm rad}^{\rm tot}$, because the rest have too low an interaction probability or lie in a spectral range where the photon density is small.

In order to calculate the total line acceleration, we have to sum up all individual contributions:

$$\begin{aligned} g_{\rm rad}^{\rm tot} &= \Sigma_{\rm thin}\, g_{\rm rad}^{\rm i} + \Sigma_{\rm thick}\, g_{\rm rad}^{\rm i} \\ &= \frac{1}{4\pi r^2 c^2} \left(\Sigma_{\rm thin}\, L_\nu \nu_{\rm i} \frac{\mathrm{d}v}{\mathrm{d}r} \frac{\tau_{\rm i}}{\rho} + \Sigma_{\rm thick}\, L_\nu \nu_{\rm i} \frac{\mathrm{d}v}{\mathrm{d}r} \frac{1}{\rho} \right) \end{aligned} \tag{15.10}$$

(with the above scheme of dividing the lines into just two categories of optical depth).

In the so-called 'Sobolev' approximation:

$$\tau_{\rm i} = \frac{k_{\rm i} \rho}{\mathrm{d}v/\mathrm{d}r} \tag{15.11}$$

the optical depth of a line can be expressed as a function of the velocity gradient, density and a 'line-strength' parameter $k_{\rm i}$ which includes all of the atomic and plasma physical details of the transition (most importantly, occupation number of the absorbing level and the interaction cross-section), and remains roughly constant throughout the wind.

The mammoth task of including thousands of atomic transitions in the summations in eq. 15.10 is made very much easier by the fact that the

distribution of line strengths can be satisfactorily approximated by an analytical power-law:

$$\mathrm{d}N(\nu, k_\mathrm{i}) = -N_0\, f_\nu(\nu)\, k_\mathrm{i}^{\alpha-2}\, \mathrm{d}\nu\, \mathrm{d}k_\mathrm{i}\,. \tag{15.12}$$

Here, $\mathrm{d}N(\nu, k_\mathrm{i})$ is the number of lines in the frequency interval $\nu, \nu+\mathrm{d}\nu$ with line strengths $k_\mathrm{i}, k_\mathrm{i} + \mathrm{d}k_\mathrm{i}$, and the exponent α takes the values $0 < \alpha < 1$. Note that the frequency distribution of lines is independent of the line strength distribution. The validity of eq. 15.12 is confirmed by detailed model atmosphere calculations, which also indicate that typically $\alpha \approx 2/3$.

Equations 15.12 and 15.10 then lead to a rather simple expression for the total line acceleration in the wind:

$$g_\mathrm{rad}^\mathrm{tot} = \mathcal{C}\, \frac{L}{4\pi r^2} \left(\frac{\mathrm{d}v/\mathrm{d}r}{\rho} \right)^\alpha \tag{15.13}$$

where $L = \int L_\nu \mathrm{d}\nu$ is the stellar luminosity. Note that in this formulation the line acceleration depends only on hydrodynamical quantities apart from the scaling factor $\mathcal{C}$ and the exponent α.[2]

15.4.3 Solving the Equation of Motion

With the simple analytical form for the total line acceleration given by eq. 15.13, we can begin to examine the hydrodynamical structure of the stellar wind. The following equations apply to stationary, spherically symmetric flows:

1. **The equation of Continuity**:

$$\boxed{\frac{dM}{dt} = 4\pi r^2 \rho v} \tag{15.14}$$

2. **The equation of Momentum**:

$$\boxed{v\frac{dv}{dr} = -\frac{1}{\rho}\frac{\mathrm{d}p}{\mathrm{d}r} - g_\mathrm{grav}(1-\Gamma) + g_\mathrm{rad}^\mathrm{tot}} \tag{15.15}$$

[2]The real challenge of computer modelling of hot star winds is the calculation of these two parameters, whose values depend on the occupation numbers of all the contributing atomic energy levels.

3. **The equation of State**:

$$\boxed{p = -\rho a^2} \tag{15.16}$$

where M is the stellar mass, p is the pressure, a is the isothermal sound speed, and $g_{\rm grav}$ is the gravitational acceleration of the star. Note that this last quantity is modified by a factor $\Gamma < 1$ to take into account the acceleration due to Thomson scattering of photons off free electrons. The parameter Γ is the same *Eddington factor* already encountered in eq. 10.40:

$$\Gamma = \frac{\kappa_{es}\, L}{4\pi c\, GM} \tag{15.17}$$

with the main source of opacity κ provided by electron scattering. Radiation pressure via Thomson scattering reduces gravity by a constant factor. For this reason, the term $M(1-\Gamma) \equiv M_{\rm eff}$ is sometimes referred to as the 'effective mass'. Clearly, $\Gamma < 1$ for a star to be stable against radiation pressure (as already discussed in Lecture 10.6); in early-type supergiants, $\Gamma \simeq 0.5$ typically.

Let us now solve these equations for the major, supersonic portion ($v > a$) of the wind. In this regime, pressure forces can be neglected. Inserting (15.14) into (15.15) and making use of (15.13), the equation of motion of the wind now becomes:

$$r^2 v \frac{{\rm d}v}{{\rm d}r} = -GM(1-\Gamma) + \mathcal{C}' L \left(\frac{{\rm d}M}{{\rm d}t}\right)^{-\alpha} \left(r^2 v \frac{{\rm d}v}{{\rm d}r}\right)^{\alpha} . \tag{15.18}$$

Equation 15.18 can be readily solved with the substitution $z = r^2 v {\rm d}v/{\rm d}r$. The parameter z needs to be constant throughout the wind to allow for a unique solution, since all the other quantities are constant as well. This constrains the mass loss rate ${\rm d}M/{\rm d}t \equiv \dot{M}$ to:

$$\dot{M} \propto L^{1/\alpha} \left[M(1-\Gamma)\right]^{1-1/\alpha} . \tag{15.19}$$

Furthermore, from the condition $z =$constant, the velocity law is obtained via a simple integration, *independently of the mass loss rate*:

$$v(r) = v_\infty \left(1 - \frac{R_*}{r}\right)^{1/2} \tag{15.20}$$

and

$$v_\infty = \left(\frac{\alpha}{1-\alpha}\right)^{1/2} \left(\frac{2GM(1-\Gamma)}{R_*}\right)^{1/2} \tag{15.21}$$

where R_* is the stellar radius. The second term on the r.h.s. of eq. 15.21 is the photospheric escape velocity. We mentioned earlier that detailed model atmosphere calculations indicate that values of $\alpha \approx 2/3$ are typical; thus, $v_\infty \simeq \sqrt{2}\, v_{\rm esc}$.

The above analytical treatment of the hydrodynamics of stellar winds has of necessity made a number of simplifying assumptions. More detailed analyses, however, do not change the picture dramatically. Most importantly, the scaling relation for $\dot{M}$ remains unaltered and the proportionality between v_∞ and $v_{\rm esc}$ is maintained, although the constant of proportionality changes somewhat. The most severe change concerns the shape of the velocity field:

$$v(r) = v_\infty \left(1 - \frac{R_*}{r}\right)^\beta \tag{15.22}$$

with the exponent $\beta \approx 0.8$ in most cases, rather than the value of 1/2 deduced above. That is, the wind velocity increases more slowly with distance from the star.

It was stated earlier (Section 15.3.2) that from the shape of the P Cygni profiles it is possible to infer the shape of the velocity field within the wind. We can now illustrate the dependence of the line profiles on the value of the exponent β in eq. 15.22 with the computed P Cygni lines shown in Figure 15.10.

The higher the value of β, the further from the star is v_∞ reached. Figure 15.10 shows that the shallower the velocity field, the stronger is the P Cygni emission. The variation in the line profiles within each panel (i.e. for the same value of β) illustrates the dependence of the emission/absorption on the ion density, which was assumed to be proportional to the total wind density. Each profile differs by a factor of ten in density. Note that the last two cases are essentially indistinguishable, because the lines have become saturated.

15.4.4 The Wind-Momentum Luminosity Relation

The scaling relations we have derived provide a theoretical explanation for the empirical relationship between wind momentum and stellar luminosity first formulated by Rolf Kudtrizki and collaborators on the basis of observations of massive stars.

In Galactic supergiants, the wind-momentum luminosity relation takes the form:

$$\dot{M} v_\infty \left(\frac{R_*}{R\odot} \right)^{1/2} \propto L^{1.46} \,. \tag{15.23}$$

What this empirical relation tells us is that, for a given stellar radius, the wind-momentum rate depends on some power of the stellar luminosity alone. On the other hand, from our theoretical scaling relations we would

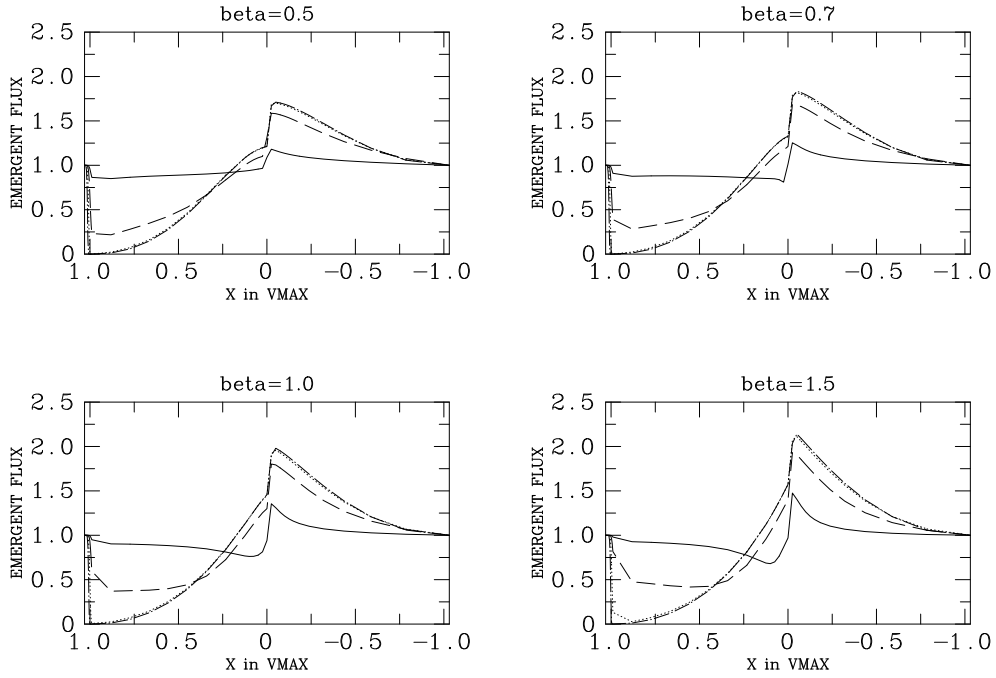

Figure 15.10: Examples of theoretical P Cygni line profiles. The four panels correspond to different values of the exponent β in eq. 15.22, which governs the steepness of the velocity law. In each panel, four profiles are shown for different optical depths of the absorbing ions, as follows. *Continuous line*: low ion column density; *dashed line*: intermediate ion column density; *dotted and dash-dotted lines:* high column densities (these last two lines are superimposed and therefore cannot be readily distinguished in the plots).

predict, combining eqs. 15.19 and 15.21:

$$\dot{M} v_\infty \left(\frac{R_*}{R_\odot} \right)^{1/2} \propto L^{1/\alpha} \, [M(1-\Gamma)]^{3/2-1/\alpha} \tag{15.24}$$

which at first glance seems quite different in that it includes an additional mass dependence. But, recalling that $\alpha \approx 2/3$, the terms in square brackets in eq. 15.24 becomes unimportant, leaving only the term $L^{1/\alpha} = L^{\sim 1.5}$ on the r.h.s. of the equation, in excellent agreement with the empirical relation at (15.23).

Summarizing, the observed wind-momentum luminosity relation can be explained as a consequence of the scaling relations for line-driven winds, plus the exponent of the line-strength distribution function being close $\alpha = 2/3$.

15.5 Metallicity Dependence of Mass Loss

From the discussion in Section 15.4, it should be fairly obvious that the properties of radiatively driven winds are likely to exhibit a metallicity dependence.

Due to its definition, the 'line-strength' parameter k_i in the Sobolev approximation (eq. 15.11) scales with metallicity (under the assumption that the ionisation balance is not severely modified) as:

$$k_{\mathrm{i,Z}} = k_{\mathrm{i,Z}\odot} \, \frac{Z}{Z_\odot} \tag{15.25}$$

Thus, the major effect of changing the metallicity is a horizontal shift of the corresponding line-strength distribution function (in the log–log representation) to the 'left' (for $Z/Z_\odot < 1$) or to the 'right' (for $Z/Z_\odot > 1$), as sketched in Figure 15.11. Such a shift translates to a change in the total number of lines contributing to the wind acceleration, and to the corresponding normalisation constant N_0 in eq. 15.12. For a power-law, the normalisation varies as:

$$N_{0,Z} = N_{0,Z_\odot} \left(\frac{Z}{Z_\odot} \right)^{1-\alpha} \tag{15.26}$$

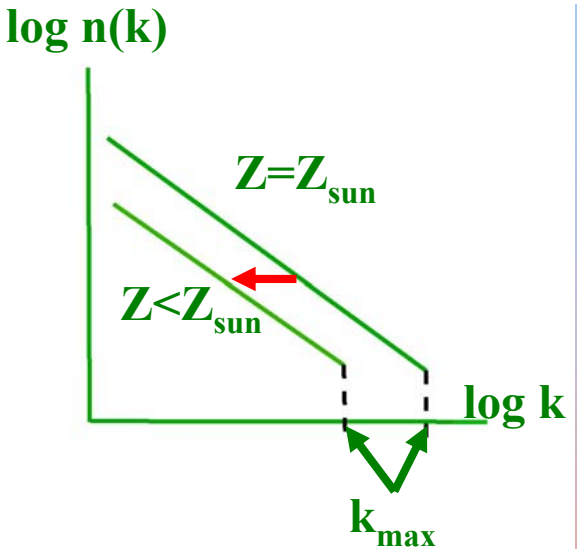

Figure 15.11: Sketch of the effect of decreasing metallicity on the line-strength distribution function.

The overall effect is a metallicity dependence of the mass loss rate of the form:

$$\dot{M}_Z = \dot{M}_{Z_\odot} \left(\frac{Z}{Z_\odot} \right)^{\frac{1-\alpha}{\alpha}} \tag{15.27}$$

or

$$\frac{\dot{M}_Z}{\dot{M}_{Z_\odot}} = \left(\frac{Z}{Z_\odot} \right)^{0.5} \tag{15.28}$$

if $\alpha = 2/3$. Metallicity has a smaller effect on the wind terminal velocity:

$$v_\infty \propto \left(\frac{Z}{Z_\odot} \right)^{0.15} \tag{15.29}$$

More extensive parameterizations of the mass loss rate as a function of L, M, $T_{\rm eff}$, v_∞ and Z have been computed from ever-more sophisticated numerical modelling (e.g. Vink et al. 2001, A&A, 369, 574). When combined with a theoretical M-L relation for massive stars, we find the typical values listed in Table 15.2. Massive stars with $M > 50 M_\odot$ lose more than 10% of their mass while on the Main Sequence.

For Galactic stars, the empirical relationship proposed by Jager et al. (1988):

$$\log \dot{M} = -8.158 + 1.769 \log(L/L_\odot) - 1.676 \log(T_{\rm eff}/{\rm K}) \tag{15.30}$$

is often adopted. Note the inverse temperature dependence. The reason is to be found in the lower opacities at higher temperatures; thus, at a given

bolometric luminosity, an A-type supergiant will have a higher mass loss rate than an O-type star.

Table 15.2 Parameters of Massive Stars

$M_{\rm ZAMS}$ $(M_\odot)$	$\log(L/L_\odot)$	$\log(\dot{M}/M_\odot\ {\rm yr}^{-1})$	$t_{\rm MS}$ $(10^6\,{\rm yr})$	$\Delta M/M^{\rm a}$
25	4.85	−6.97	6.6	0.028
40	5.34	−6.23	4.5	0.067
60	5.70	−5.68	3.7	0.13
85	5.98	−5.26	3.3	0.21
120	6.23	−4.88	2.8	0.31

[a] Fractional mass lost while on the Main Sequence

Both eq. 15.30, scaled for metallicity according to eq.15.28, and the multi-parameter theoretical formulation of the mass loss rate by Vink et al. (2001) do a reasonably good job of matching the data (Figure 15.12), although there remains significant scatter ($\sim 0.3\,$dex), some of it undoubtedly due to uncertainties in the measurements of $\dot{M}$.

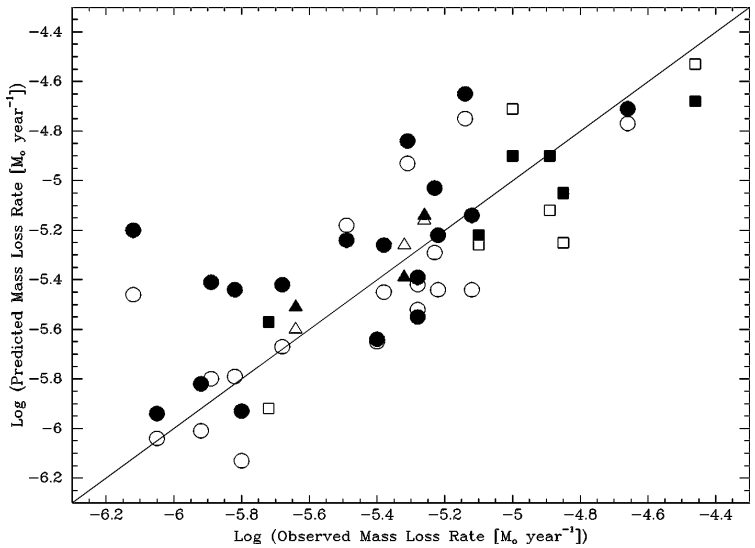

Figure 15.12: Comparison between observed (x-axis) and predicted (y-axis) mass loss rates. Open symbols denote values of $\dot{M}$ calculated from eq. 15.30 with the metallicity scaling of eq. 15.28, while filled symbols are those given by the theoretical formalism of Vink et al. (2001). Circles are Galactic stars, squares LMC stars, and triangles SMC stars. (Figure reproduced from Massey et al. 2003, ARAA, 41, 15).

We still have much to learn regarding how mass loss rates in massive stars vary with metallicity and perhaps other parameters of the host galaxy. Our knowledge of this field is improving with observations, made possible by 8-10 m telescopes, of individual massive stars in galaxies beyond the Local Group, as well as in low-mass, low-metallicity dwarf galaxies in the Local Group. It is important to remember that the metallicity dependence of mass loss rates, as given for example by eq. 15.28, is empirically untested for metallicities $Z \lesssim 1/6 Z_{\odot}$ (the metallicity of SMC O-type stars). This is crucial when we come to consider the evolution of the 'First Stars' (also referred to as Population III stars), which formed out of primordial gas—consisting only of H and He—and were likely very massive.